International Journal of Nanomedicine

Dovepress
Taylor & Francis Group

Open Access Full Text Article

ORIGINAL RESEARCH

Impact of Cerium Doping on the Osteogenic Properties of a 3D Biomimetic Piezoelectric Scaffold with Sustained Mg^{2+} Release

Kai Kang, Xiyuan Qin, Jiaqi Pan, Tianyu Zhang, Xincong Li, Hai Zhuang, Shoushan Bu

Department of Stomatology, First Affiliated Hospital of Nanjing Medical University, Nanjing, People's Republic of China

Correspondence: Shoushan Bu, Email bushsh@vip.sina.com

Background: In the realm of bone tissue engineering, the role of biomimetic piezoelectric scaffolds made from whitlockite (WH) nanoparticles is increasingly recognized. WH, the second most abundant mineral in human bone, possesses piezoelectric properties and the capacity to release magnesium ions (Mg^{2+}), both of which are vital for osteogenic differentiation. This study investigates the osteogenic effects of cerium (Ce) doping on three-dimensional biomimetic piezoelectric scaffolds composed of whitlockite (WH) nanoparticles.

Methods: WH nanoparticles with varying Ce concentrations were synthesized and scaffolds were prepared using a freeze-drying process with sodium alginate as the matrix. In vitro experiments with human bone marrow mesenchymal stem cells (hBMSCs) assessed cell proliferation and differentiation, while animal studies employed a rat calvarial defect model to evaluate new bone formation and mineralization.

Results: Our findings revealed that Ce doping modifies the crystallinity and electrical properties of WH nanoparticles, thereby affecting their osteogenic potential. In vitro studies indicated that scaffolds with a Ce/Ca ratio of 0.06 significantly boosted osteogenic marker expression. Furthermore, animal studies confirmed that Ce-doped WH scaffolds, especially those with the 0.06 ratio, markedly improved both new bone formation and mineralization.

Conclusion: The study demonstrates that Ce doping can significantly enhance the osteogenic properties of WH-based scaffolds, with the optimal Ce/Ca ratio of 0.06 being particularly effective in promoting bone formation. This research provides a promising approach for the development of advanced materials in bone tissue engineering.

Keywords: whitlockite, cerium, piezoelectric scaffolds, bone tissue engineering

Introduction

The rapid advancement and interdisciplinary convergence of biology, materials science, medicine, and engineering have given rise to the innovative field of regenerative medicine.[1] This discipline seeks to reduce scar tissue formation and expansion while enhancing the regenerative potential for effective repair and functional restoration of damaged or aging tissues and organs.[2] At present, autologous bone grafting remains the gold standard for bone defect repair. However, the availability of autologous bone is limited, and complications often arise at the donor site.[3] As a significant aspect of regenerative medicine, bone tissue engineering has gained considerable attention and has become a widely studied approach for addressing congenital and acquired bone defects.[4] Clinical efforts have explored the use of artificial bone substitutes made from metals, ceramics, or polymers. Despite progress, these materials present various limitations, including challenges in biocompatibility, bioactivity, biodegradability, porosity, and mechanical compatibility with host bone.[5] Growth factors, particularly the FDA-approved bone morphogenetic proteins 2 and 7, are bioactive molecules frequently used in bone grafting to improve osteogenic responses.[6] Incorporating growth factors, such as bone morphogenetic protein-2 (BMP-2), skeleton growth factor (SGF), and transforming growth factor-β (TGF-β), into osteoinductive scaffold designs has shown promise. However, the uncontrolled and ectopic release of these growth factors frequently

Received: 16 January 2025
Accepted: 28 March 2025
Published: 6 April 2025

Graphical Abstract

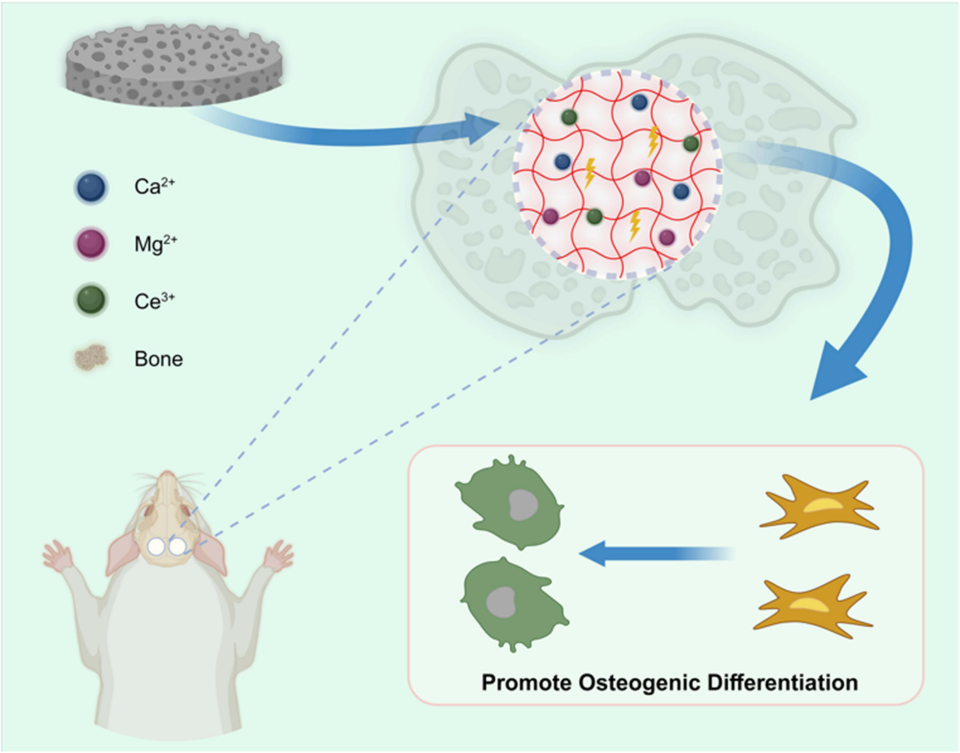

results in ectopic bone formation, compromising bone repair outcomes,[6,7] for instance, collagen-based composite grafts containing growth factors have been withdrawn from clinical use due to reported complications.[7,8] Consequently, growth factor-free bone regeneration remains a key challenge, particularly in the domain of craniofacial engineering. Thus, there is an urgent demand for innovative scaffolds with multifunctional biological properties to facilitate effective bone defect reconstruction.

Whitlockite (WH, $Ca_{18}Mg_2(HPO_4)_2(PO_4)_{12}$) is the second most abundant mineral in human bone, comprising approximately 20–35 wt% of the total inorganic composition.[9,10] Studies on WH have demonstrated its ability to promote the osteogenic differentiation of human bone marrow mesenchymal stem cells (hBMSCs) through the controlled release of magnesium ions (Mg^{2+}).[11,12] Due to its favorable biological properties, WH has received increasing attention as a scaffold material in tissue engineering. Research has shown that WH effectively releases Mg^{2+} ions during degradation, which induces and supports osteogenic differentiation and neoblastogenesis,[13–19] reduces osteoclast activity,[20,21] promotes neoangiogenesis,[22,23] and exhibits antimicrobial[24] and hemostatic properties.[25,26] As a crucial base material for degradable bone repair scaffolds, comparative studies by Jang et al on the ex vivo and in vivo biocompatibility of WH, HAP, and β-TCP demonstrated that Mg-WH-containing scaffolds promoted bone-specific differentiation more effectively than HAP-containing composites. Additionally, WH implants induced bone regeneration comparable to, or even superior to, HAP and β-TCP implants in a rat cranial defect model.[27] Furthermore, the synthesis method for WH developed by this research team continues to be widely referenced in the literature.[11,28] Bauer et al reported that WH particles promote cell proliferation and osteogenic differentiation while inhibiting osteoclast activity to a greater extent than hydroxyapatite [HAP: $Ca_{10}(PO_4)_6(OH)_2$]. Scaffolds with a 70:30 ratio of HAP to WH, prepared as 5 mm diameter constructs, demonstrated excellent osteogenic properties.[29]

Endogenous electric fields naturally exist in the human body and play a vital role in bone development and regeneration.[30] The application of electrically active biomaterials circumvents the uncertainties associated with drug loading, delivery, and bioavailability when compared to approaches involving growth factors, cytokines, or other pharmaceuticals.[31] Consequently, piezoelectric and electroactive bone implants have attracted significant attention due to their ability to generate inherent electrical signals. Piezoelectric materials inherently possess a non-centrosymmetric crystal structure, characterized by the spatial separation of positive and negative charge centers. This unique structural feature enables the generation of electric polarization under mechanical stress, as the applied force induces a reorientation of internal electric dipole moments, thereby exhibiting the characteristic piezoelectric effect.[32] However, such implants often lack bioactivity, bioresorbability, and components resembling the ECM. WH is an Mg-doped calcium phosphate that is capable of gaining piezoelectricity after sintering with water loss and crystal domain transition. In 2021, Kaliannagounder et al demonstrated that WH nanoparticles annealed at 750°C (PWH-750) exhibited remarkable electroactivity. In vitro studies on cell proliferation and differentiation showed that piezoelectric WH nanoparticles could stimulate mechanosensitive ion channels PieZo1 and TRPV4 under LIPUS conditions, leading to improved cellular proliferation.[33] Building on these findings, Wang et al in 2022 incorporated WH electroactivity into PCL-based 3D-printed bone tissue engineering scaffolds. Their study revealed that PWH scaffolds displayed excellent biocompatibility and safety while outperforming β-TCP and non-electroactive WH scaffolds in promoting bone, vascular, and neural regeneration.[22]

Lead-free piezoelectric biocompatible ceramics, such as barium titanate (BTO), zinc oxide (ZnO), hydroxyapatite (HAP), barium-zirconium titanate-calcium barium titanate (BZT-BCT), bismuth ferrite (BFO), lithium niobate (LN), and potassium niobate (KNN), have been developed to emulate the natural piezoelectricity of bone. Among these, potassium sodium niobate (KNN) has become a prominent research focus in tissue engineering.[31,33–35] Despite their high biocompatibility, most piezoelectric ceramics, except HAP, are biologically inert, limiting their applicability as bone-filling ceramics in biological implants. This limitation improves the significance of studying and applying WH piezoelectric activity.

Rare earth elements, recognized as critical strategic resources, impart exceptional ex vivo and in vivo properties to implantable bone regeneration materials. These include improving mechanical properties, enabling material visualization, inducing cellular responses, and modulating the local microenvironment, making them a focus of extensive research in biomedicine and materials science.[36] Cerium, one of the most active rare earth elements, exhibits diverse physiological and biochemical effects due to its chemical similarity to calcium.[37] The incorporation of CeO_2 into biopolymers has been widely studied, yielding valuable applications in areas such as drug delivery, bioscaffolds, and biomedicine.[38–40] For instance, gelatin-sodium alginate-cerium oxide nanocomposite scaffolds containing $nCeO_2$ have been shown to significantly improve bone repair.[41] Kalyanaraman et al evaluated the biosafety of $nCeO_2$ by monitoring changes in local tissues and major organs after 28 days of subcutaneous implantation in rats. Their findings demonstrated that $nCeO_2$ caused no adverse effects on vital organs and did not induce significant local tissue irritation, confirming its safety.[42] Similarly, a study by Xu et al revealed that $nCeO_2$ nanoparticles exhibited excellent biocompatibility, supporting cell proliferation even at high concentrations (1000 μg/mL).[43] CeO_2 has also shown promise in promoting osteogenic differentiation of MSCs and encouraging the formation of mineralized nodules when incorporated into calcium silicate coatings.[44] Furthermore, Xiang et al reported that CeO_2 nanoparticles significantly accelerated angiogenesis by increasing intracellular free Ca^{2+} levels, stabilizing HIF-1α, and elevating VEGF expression.[45] Additionally, Zhang et al explored a three-dimensionally printed scaffold fabricated by integrating cerium oxide nanoparticles into bioactive glass, which enables sequential therapeutic effects on inflammation and promotes osteogenesis in bone defects.[46] Given these findings, further systematic investigation into the osteogenic properties and bioelectrical activities of composite scaffolds integrating Ce elements with pWH nanoparticles is warranted. This research focuses on the impact of composite scaffolds of pWH nanoparticles with varying Ce doping levels on osteogenic properties and biosafety. To avoid interference from hydrogel materials with high bioactivity and potential interactions with Ce ions, we selected sodium alginate (Alg) hydrogel as the scaffold matrix. Alg hydrogel is a simpler, biocompatible, and safe material, ensuring the reliability of experimental outcomes.

Materials and Methods

Chemicals and Materials

Alginic acid sodium salt with low viscosity (50 mPa.s (1%, 20°C)) was supplied by Macklin. Calcium hydroxide (CaH_2O_2; MW 74.09 g/mol, 95% purity) was purchased from Acmec, while cerium (III) nitrate hexahydrate (Ce(NO3)3·6H2O; MW 434.22 g/mol, 99.5% purity) was provided by Heowns. Magnesium hydroxide (MgH_2O_2, MW 58.32 g/mol, 98% purity) and calcium chloride ($CaCl_2$; MW 110.98 g/mol, 99.5% purity) were both obtained from Macklin. Water was purified using reverse osmosis (resistivity >18 MΩ·cm; Milli-Q, Millipore®, Madrid, Spain).

Preparation of pWH, pWH-Ce-0.03, pWH-Ce-0.06, pWH-Ce-0.09 Nanoparticles and pWH/Alg, pWH-Ce-0.03/Alg, pWH-Ce-0.06/Alg, pWH-Ce-0.09/Alg Scaffolds

Based on previously published methods,[11] Whitlockite ($Ca_{18}Mg_2(HPO_4)_2(PO_4)_{12}$) nanoparticles were synthesized via a chemical precipitation approach. Briefly, 0.77 M calcium hydroxide ($Ca(OH)_2$) and 0.23 M magnesium hydroxide ($Mg(OH)_2$) were added to DI water and heated to 100°C under constant stirring. After an additional 30 minutes of vigorous stirring, an equal volume of 0.95 M phosphoric acid (H_3PO_4) was added dropwise to the solution at a rate of 12.5 mL/min. The mixture was aged at room temperature for 12 hours after a 10-hour reaction period. The precipitate was then collected via centrifugation at 4000 rpm for 5 minutes, washed several times with DI water, dried at 60°C for 48 hours, and pulverized. To prepare WH-Ce nanoparticles with different cerium doping levels (Ce/Ca molar ratios of 0.03, 0.06, and 0.09), cerium nitrate was added to the calcium hydroxide and magnesium hydroxide mixture in appropriate proportions. All nanoparticles were annealed at 750°C in a muffle furnace for 3 hours to obtain piezoelectric pWH, pWH-Ce-0.03, pWH-Ce-0.06, and pWH-Ce-0.09 nanoparticles.

For scaffold preparation, pWH-Ce-0.03, 0.06, or 0.09 nanoparticles (1% w/v) were dispersed in DI water. Sodium alginate powder (5% w/v) was gradually added to the solution while stirring vigorously at 60°C. After 2 hours of stirring, the mixture was transferred into 6-well or 96-well plates. A calcium chloride solution (1% w/v) was then carefully injected into the plates to crosslink the alginate. After 12 hours of crosslinking, the scaffolds were immersed in distilled water for another 12 hours, followed by freeze-drying at −80°C for more than 48 hours. The pWH/Alg scaffolds were prepared under identical conditions without cerium doping. For ease of reference, the scaffold groups (pWH/Alg, pWH-Ce-0.03/Alg, pWH-Ce-0.06/Alg, and pWH-Ce-0.09/Alg) will henceforth be referred to as groups 0, 0.03, 0.06, and 0.09, respectively.

Characterization

X-ray diffraction (XRD; D2 PHASER, Bruker, Germany) was performed to confirm the structural characteristics of all samples, using Cu-Kα radiation. The scanning speed was set to 10°/min over a 2θ range of 3–90°. Fourier transform infrared spectroscopy (FTIR; iS20, ThermoFisher, USA) was utilized to identify functional groups within the wavenumber range of 4000–500 cm^{-1}. Morphologies were observed using a scanning electron microscope (SEM, Regulus8100, Hitachi, Japan), while energy dispersive spectroscopy (EDS) was employed for surface element analysis. To evaluate the electrical properties of the nanoparticles, hydrogel films were trimmed to dimensions of 10×15 × 1 mm after synthesis. These films were subjected to cyclic voltammetry (CV) curve characterization. The compressive strengths of the scaffolds (1.0 × 1.0×1.0 cm) were measured using a microcomputer-controlled electronic universal testing machine (WDW, Instron 5967 (10 KN), USA) at a compression speed of 1 mm/min. For in vitro studies on ion release and degradation, scaffolds were immersed in ultrapure water at 37 °C. The concentrations of cerium (Ce), magnesium (Mg), and calcium (Ca) in the immersion medium were determined at specific time points using inductively coupled plasma optical emission spectrometry (ICP; iCAP 7000, Thermo Fisher). The degradation rate of the nanohybrid scaffolds (V) was calculated using the following equation:

$$V = (W_0 - W_1)/W_0 \quad (1)$$

where W_0 was the initial nanohybrid scaffold weight and W_1 was the scaffold weight after 7 days of soaking.

Porosity (P) was calculated with the following equation:

$$P = \frac{W_1 - W_0}{\rho V_0} \times 100\% \quad (2)$$

where W_0 was the dry weight of composite scaffolds, W_1 was the weight of scaffolds after being soaked in ethanol, ρ was the density of ethanol (20 °C, ρ=0.790 g/mL), and V_0 was the volume of scaffold.

Swelling rate (SR) was obtained from the following equation:

$$SR = (W_1 - W_0)/W_0 \quad (3)$$

where W_0 was the original weight of scaffolds, and W_1 was the weight of scaffolds after soaking in DI water for 24 hours at 37°C.

In vitro Cell Experiments

hBMSCs were procured from ZQXZbio. To prepare scaffold extracts, according to the standard of ISO 10993,[47] two scaffold samples (31.2 mg) were immersed in 0.5 mL of α-MEM and incubated at 37°C for 24 hours. The resulting solution was then collected and filtered through a 0.22-μm filter (Millipore, USA). The scaffold extracts were supplemented with 10% FBS, 100 U/mL penicillin, 100 μg/mL streptomycin, 100 μM dexamethasone, 10 mm β-glycerophosphate, and 50 μM ascorbate-2-phosphate to a final volume of 12 mL, forming the pWH/Alg-OM and pWH-Ce/Alg-OM media. Control medium without scaffold extracts was also prepared.

A Cell Counting Kit-8 (CCK-8) assay (Beyotime Biotechnology, China) was used to assess cell proliferation and cytotoxicity on nanohybrid scaffolds. hBMSCs (1.5×10^4 cells/cm²) were seeded onto WH/CS and Ce-WH/CS scaffolds and incubated in 96-well plates for 2, 4, and 6 days. The optical density (OD) at 450 nm was measured using a microplate reader. On day 3, cell viability was further evaluated using calcein-AM/PI staining (Solarbio, China). Fluorescence images were captured with an inverted fluorescence microscope, with live cells appearing green and dead cells appearing red. Cell adhesion and morphology on the scaffolds were examined as previously reported[48] by staining nuclei with DAPI (Antifade Mounting Medium, P0131, Beyotime Biotechnology, China) and F-actin with phalloidin (Actin-Tracker Red-594, Beyotime Biotechnology, China). Stained samples were fixed and imaged using an inverted fluorescence microscope (DMI3000B, Leica, Germany).

To investigate osteogenic differentiation, hBMSCs were cultured in conditioned media (CM) until confluence was reached. Subsequently, osteogenic medium (OM) was introduced. On day 7, alkaline phosphatase (ALP) staining was conducted following the manufacturer's instructions (Beyotime). On day 14, cells were stained with 40 mm Alizarin Red S (ARS) solution (Beyotime) for 20 minutes at room temperature (20–26°C) to evaluate mineralized nodule formation. Quantitative real-time polymerase chain reaction (RT-PCR) was performed on day 7 to measure the expression levels of osteogenic genes, including alkaline phosphatase (ALP), collagen type I (COL-I), and osteopontin (OPN). Primer sequences are provided in Table S1. Additionally, Western blot analysis was conducted to assess the expression of osteogenic proteins, following standard protocols. Each experiment was repeated independently three times.

Animal Experiments

All animal experiments described in this study were conducted under constant temperature and humidity and in accordance with guidelines approved by the Institutional Animal Care and Use Committee of Nanjing Medical University (IACUC-2307035, Nanjing, China). Twenty male Sprague-Dawley rats (8 weeks old, weighing 200–250 g) were used to establish a critical-size skull defect model with a 5-mm diameter defect. The rats were randomly divided into five groups, each receiving a different scaffold implant: (1) Blank, (2) Group 0, (3) Group 0.03, (4) Group 0.06, and (5) Group 0.09. The scaffolds were prepared with a diameter of 5 mm and a thickness of 1 mm. At both 4 and 8 weeks after implantation, two rats from each group were humanely euthanized using isoflurane anesthesia (2% in 100% oxygen). Following anesthesia, skull samples were carefully excised along with the surrounding tissues and fixed in 4% formalin for 24 hours. All specimens underwent scanning and analysis using a Micro-CT scanner (SkyScan1176, Bruker, Germany). The region of interest (ROI) was defined as a cylindrical volume with a diameter of 5 mm and

a height of 1 mm using dedicated analysis software. Relative bone volume to tissue volume (BV/TV) and local bone mineral density (BMD) were quantified. Hematoxylin-eosin (H&E) staining, Masson's trichrome staining (Biosharp, China), and immunohistochemistry (IHC) analysis were performed on consecutive tissue sections. Images were scanned using a Nikon Eclipse E600 microscope for further evaluation.

Statistical Analysis

All quantitative data are presented as mean ± standard deviation. Statistical significance was determined using one-way analysis of variance (ANOVA) followed by Tukey's post-hoc test. A p-value less than 0.05 was considered statistically significant (*$p < 0.05$, **$p < 0.01$, ***$p < 0.001$, and ****$p < 0.0001$).

Results and Discussion

Characterization of Nanoparticles and Scaffolds

In this study, Figure 1a illustrates that nanoparticles were successfully synthesized using a chemical precipitation method and subsequently annealed in a muffle furnace to impart piezoelectric properties.[33] Freeze-dried hydrogel scaffolds doped with these inorganic nanoparticles were then developed, demonstrating the continuous release of bioactive ions (Mg^{2+}, Ca^{2+}, Ce^{3+}) along with piezoelectric functionality. SEM and EDS analyses were conducted to examine the morphology and composition of the nanoparticles. As shown in Figure 1d, WH nanoparticles exhibited uniformly dispersed rhombohedral shapes with an approximate size of 50 nm, which matched well with previously reported results.[18] When cerium was introduced, WH-Ce nanoparticles displayed irregular shapes with sizes ranging from 20 to 50 nm. Doping with rare earth elements will change the chemical properties of the nanoparticle surface, including surface charge and functional groups, which affects how the particles interact and can cause them to clump together. This clumping makes the particles less uniform in shape and size.[49] Additionally, rare earth elements alter the nanoparticles' surface energy. The uneven distribution of REE ions on the particle surface leads to local differences in surface energy, with high surface energy regions promoting particle growth and low surface energy regions inhibiting particle growth, thus affecting the morphology and particle size distribution of composite nanoparticles.[50] EDS point spectra of the WH-based composite nanoparticles (Figure 1d) confirmed the presence of Ca, Mg, O, P, and Ce, aligning with the SEM images. By contrast, the EDS spectrum of pure WH nanoparticles showed signals only from Ca, Mg, O, and P, consistent with the absence of cerium in their composition. For WH-Ce-0.03, WH-Ce-0.06, and WH-Ce-0.09 nanoparticles, the EDS results confirmed cerium content of 2.7, 6.1, and 8.2 wt.%, respectively, which matched with theoretical values. Figure 1b presents the XRD diffractograms for all nanoparticle samples, showing peaks consistent with crystalline phases and referencing PDF#70-2064/PDF#00-042-0578 within the 2θ range of 15–45°. The diffraction peaks at 17.26°, 26.09°, 28.16°, 31.38°, and 34.79° corresponded to crystal planes (110), (1010), (214), (0210), and (220), respectively.[51] While most samples exhibited no significant changes in peak positions or shapes, WH-Ce-0.09 nanoparticles displayed weakened peak intensities along with additional uncharacteristic peaks, indicating reduced crystallinity. These results suggest that Ce doping progressively reduces the lattice parameter, and higher doping concentrations inhibit the growth of WH nanoparticles, resulting in decreased crystallinity. This reduction may be attributed to the suppression of crystal growth, a critical factor influencing crystallinity, as well as the direct effects of cerium doping on nanoparticle development.[52] Specifically, as the cerium doping concentration increases, the non-uniform strain resulting from the mismatch in size between the calcium and cerium ions becomes more pronounced. In the replacement of calcium ions in the lattice, the larger cerium ions generate uniform tensile strain, which ultimately affects the crystallinity.[53] On the other hand, The growth and formation of crystals play a crucial role in determining a material's crystalline properties, and the introduction of cerium ions may interfere with the orderly arrangement of the crystal lattice in two main ways: by occupying the lattice sites or by forming defective structures, where the former hinders the directional growth of the crystal surface and the latter triggers the accumulation of lattice stresses, which ultimately lead to a decrease in the degree of crystallinity in a synergistic manner.[54] Overall, these findings confirm the successful synthesis of WH-Ce-0.03, WH-Ce-0.06, and WH-Ce-0.09 nanoparticles.

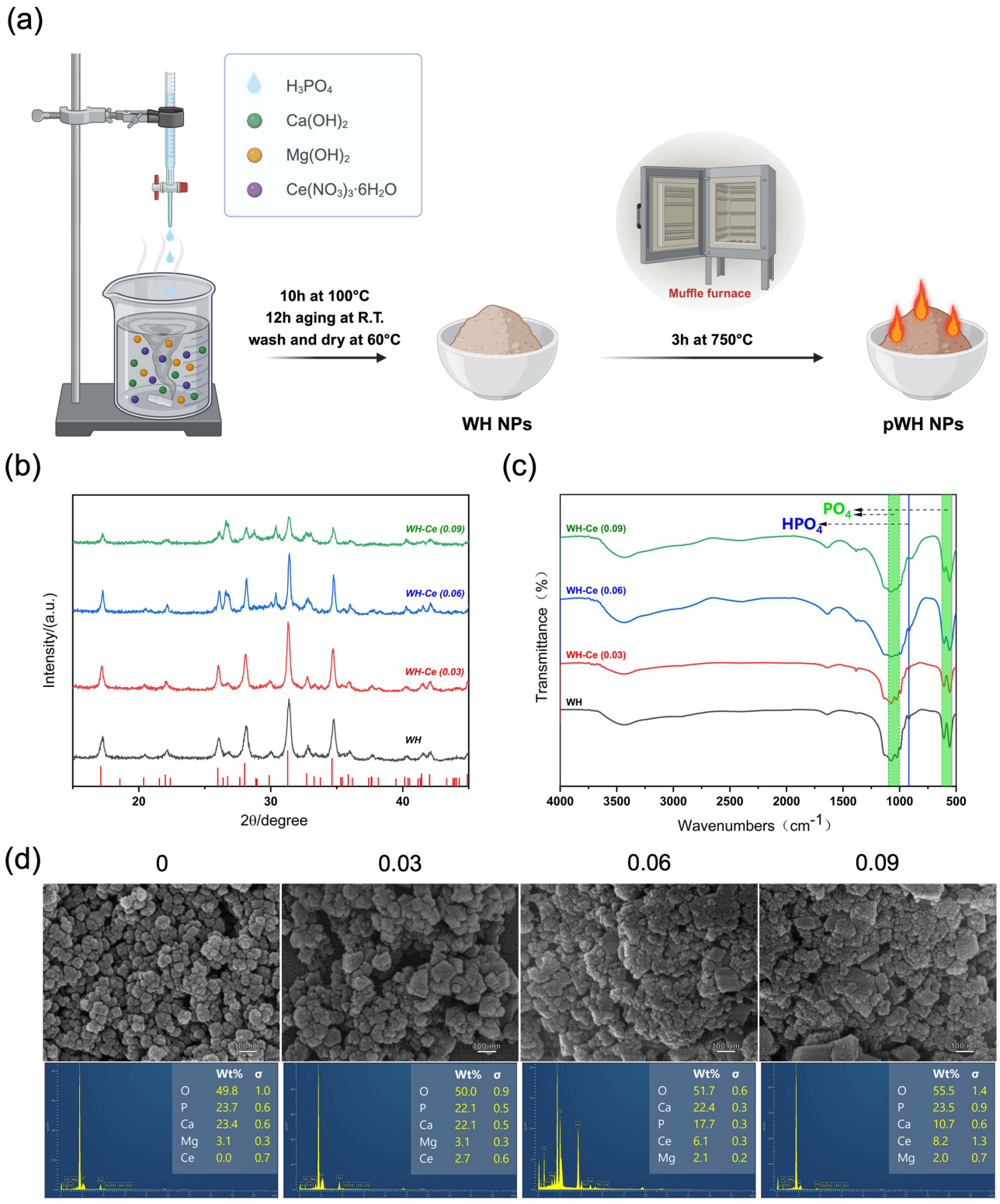

Figure 1 Preparation and characterization of different nanoparticles. (**a**) schematic showing the fabrication process of nanoparticles. (**b**) XRD patterns and (**c**) FTIR spectra of WH and WH-Ce nanoparticles with different cerium doping levels. (**d**) SEM images and corresponding EDS point spectra of WH and WH-Ce nanoparticles with different cerium doping levels.

https://doi.org/10.2147/IJN.S514047

Figure 1c presents the FTIR spectra of WH nanoparticles with varying cerium concentrations. Consistent with the XRD results, the characteristic absorption bands of all samples are clearly observed, indicating that the addition of cerium does not alter the crystal matrix. The bands in the range of 995–1073 cm^{-1} correspond to the PO_4^{3-} group, while peaks at 557 cm^{-1} and 608 cm^{-1} are attributed to the O–P–O bending vibration. The HPO_4^{2-} group is identified by the P (–OH) stretching vibration band at 918 cm^{-1}. These peaks are recognized as the characteristic features of WH as reported in previous results.[22] Additionally, the presence of a broad band in the range of 3500–3000 cm^{-1} indicates that the nanoparticle surfaces are capable of adsorbing water molecules, a property attributed to their hydrophilicity.[51]

To optimize the electrical activity of WH nanoparticles, the electrical properties of pWH/Alg film materials were evaluated following annealing treatments at 650, 700, and 750°C. As illustrated in Figure 2c, the material annealed

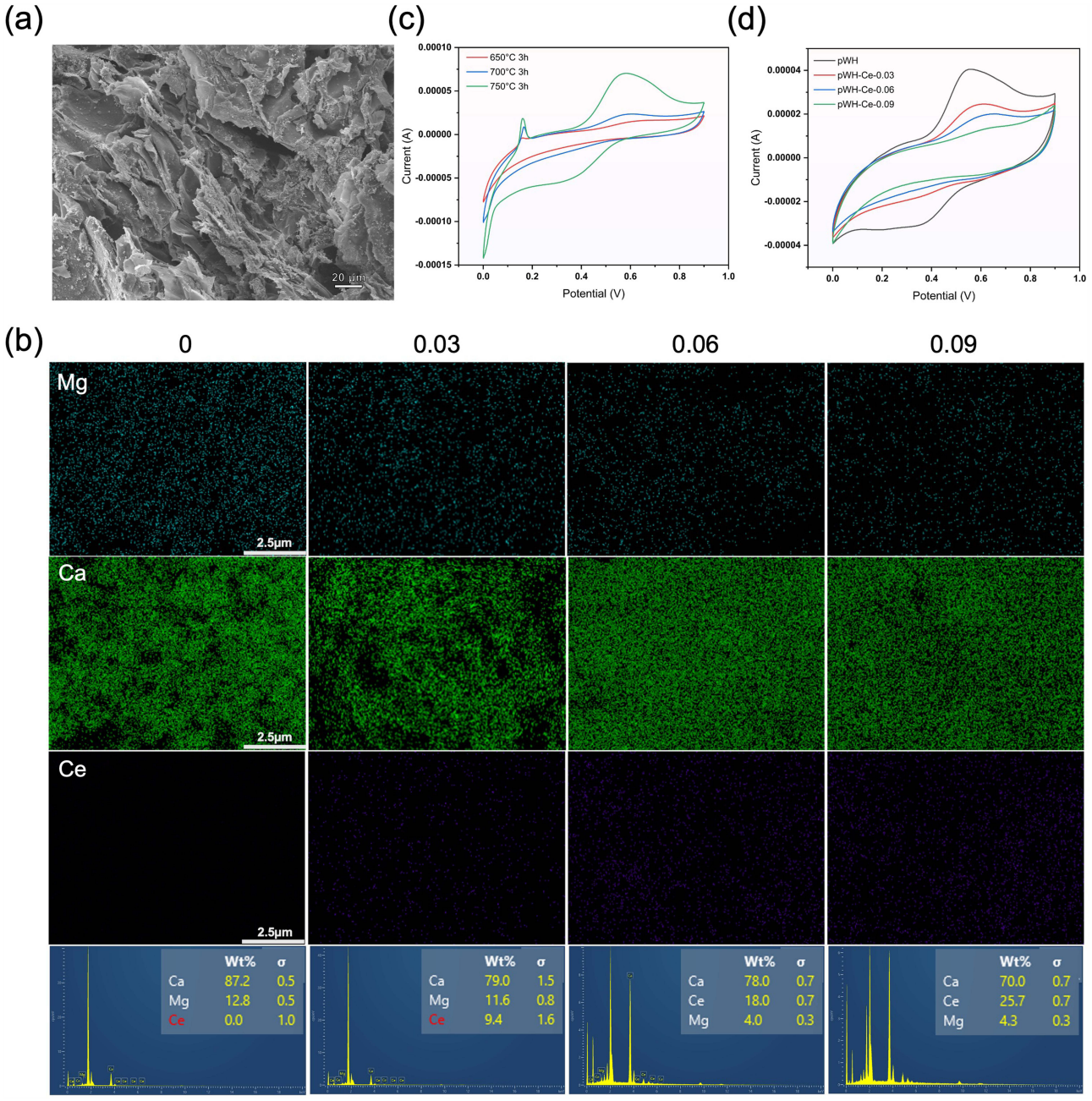

Figure 2 Characterization of composite scaffolds with different nanoparticles. (**a**) representative high-resolution SEM images. (**b**) element distribution images of Ca, Mg, and Ce and corresponding EDS spectra. (**c**) CV curves of pWH/Alg composite films under different annealing treatments (650/700/750 °C, 3 h). (**d**) CV curves of pWH/Alg, pWH-Ce-0.03/Alg, pWH-Ce-0.06/Alg, and pWH-Ce-0.09/Alg composite films under the annealing treatments (750 °C, 3 h).

at 750°C exhibited the greatest current change under the same voltage, identifying 750°C as the optimal annealing temperature. Unlike previous study that identified 650°C as the optimal temperature,[22] we believe this difference may result from using Alg instead of PCL as the matrix material for WH nanoparticles. The way WH nanoparticles spread within different matrix materials likely affects the test outcomes. Subsequently, the electrical activity of pWH/Alg, pWH-Ce-0.03/Alg, pWH-Ce-0.06/Alg, and pWH-Ce-0.09/Alg films annealed at 750°C was analyzed. Figure 2d shows a decreasing trend in electrical activity with increasing cerium doping. The incorporation of cerium appears to influence grain growth and the material's microstructure. In some cases, Ce doping can refine grains and improve homogeneity, improving piezoelectric properties.[55] Wei et al demonstrated this effect by developing cerium-doped hollow $BaTiO_3$ nanoparticles (hBTCe) to improve piezoelectric catalysis. Ce doping in hBTCe nanoparticles enhanced polarization, promoted oxygen vacancy formation, improved electron/hole separation, and reduced the band gap. The strong piezoelectric current and abundant reactive oxygen species generated under ultrasound exhibited significant antibacterial effects against planktonic bacteria and biofilms. These results highlighted the potential of Ce modulation in defective engineering and hollow structures for improving polarization, piezoelectric potential, and piezoelectric-catalyzed antimicrobial applications.[56] However, excessive Ce doping may negatively affect piezoelectric properties by inducing uneven grain growth or creating unfavorable microstructures. Cerium, with its variable ionic valence states (Ce^{3+} and Ce^{4+}) and ionic radii, can occupy either the A-site or B-site in piezoelectric materials, substituting for ions such as Pb^{2+}, Ti^{4+}, Mg^{2+}, and Nb^{5+}. These substitutions can cause lattice distortions and charge defects. Specifically, lattice distortions may create defects in the lattice, such as defective dipoles and lattice twists. These defects strongly affect the polarization and strain response within the piezoelectric ceramic material,[57] ultimately impacting the material's piezoelectric performance.[58]

SEM analysis revealed that the composite hydrogel scaffolds possessed a characteristic porous structure (Figure 2a), with nanoparticles evenly distributed across the surface of the pore walls. The spatial distribution of Ca, Mg, and Ce within the scaffolds was observed through EDS elemental analysis (Figure 2b). The elemental mapping demonstrated a uniform dispersion of these elements, and the quantitative analysis results matched well with the theoretical composition of the nanoparticles. The ideal scaffold material should possess not only a porous structure but also mechanical properties comparable to those of normal human bone tissue. To evaluate this, the compressive properties of the scaffold materials were tested. Figure 3a shows the results for freeze-dried Alg hydrogel scaffolds doped with 1% w/v nanoparticles and prepared in dimensions of 1 × 1×1 cm. As the compression ratio increased, the compressive strength of the scaffolds also increased, reaching 2.98 MPa at a compression ratio of 29.11%. This strength falls within the range of trabecular bone compressive strength (0.1–16 MPa).[59] When large pores in the scaffolds were destroyed under compression, the material exhibited ductile behavior, resulting in a sudden decrease in compressive strength followed by a gradual increase.

The in vitro ion release performance of the scaffolds is presented in Figure 3b–d. Over time, as the scaffold materials degraded in ultrapure water, Ca, Mg, and Ce ions were released and dispersed into the surrounding medium. The ion release rates varied across different time intervals, with the highest release observed during the first 24 hours. By 120 hours, the ion release and reprecipitation processes of the nanoparticles had reached a dynamic equilibrium, and the accumulated concentrations of each ion approached their maximum values, remaining within safe concentration ranges.[42,43,60] Notably, the maximum concentration of Ce ions in group 0.09 reached 1.53 μM. The ion release characteristics of the scaffolds are closely tied to their degradation properties. Using equation (1), the in vitro degradation rates of the scaffolds were calculated after 5 days of immersion in ultrapure water, yielding values of 8.37%, 10.56%, 11.78%, and 12.02% for the respective scaffold groups. Additionally, the scaffold porosity was determined to be 37.41% and the swelling rate to be 13.58 based on equations (2) and (3), respectively.

In vitro Cell Experiments

Following ISO standard 10993, scaffold extracts were prepared and incubated with hBMSCs to evaluate the biocompatibility and cytotoxic potential of the materials through fluorescence staining (Live/Dead and cytoskeleton) and the CCK-8 assay. The results of live-dead staining, illustrating the growth of cells cultured with different scaffold extracts for 3 days, are presented in Figure 4a. The cell densities across all groups were similar, with predominantly green fluorescence (live

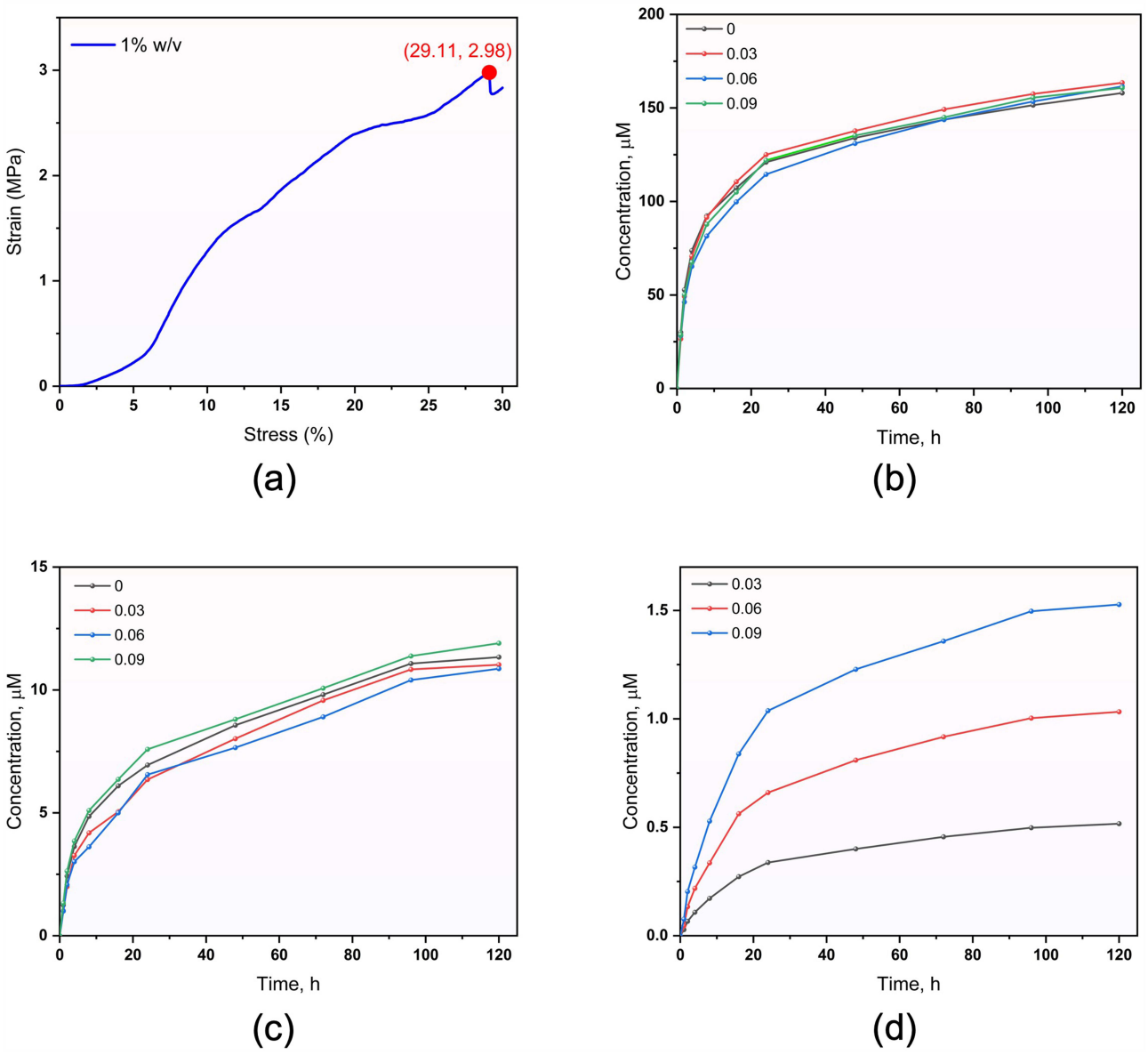

Figure 3 (**a**) compression stress-strain curve of composite scaffold. Ion release performances of composite scaffolds: (**b**) Ca; (**c**) Mg; and (**d**) Ce ions.

cells) and no significant red fluorescence (dead cells) observed, indicating the absence of cytotoxicity. Cells in each group were evenly distributed within the field of view, appeared healthy, and exhibited minimal cellular debris. As shown in Figure 4b, F-actin filaments within the cytoskeleton were stained with phalloidin (red), while cell nuclei were stained with DAPI (blue). The cytoskeleton fluorescence staining demonstrated normal cellular morphology across all groups. At higher magnification, cells in all groups were fully spread, displaying regularly arranged cytoskeletal fibers and a typical spindle morphology. The cell spreading area was comparable to that observed in the Nc group. Quantitative assessment of cell proliferation and toxicity using the CCK-8 assay (Figure 4c) revealed a progressive increase in hBMSC numbers over time in all groups. Notably, the cell count on day 6 was approximately three times higher than on day 4. The OD values among the groups showed minimal variation at all time points, with no statistically significant differences ($p > 0.9$). In summary, these results demonstrate that all scaffold groups exhibited excellent biocompatibility and similar effects on cell proliferation and compatibility when compared to the Nc group.

In this study, we investigated the osteogenic effects of pWH/Alg scaffolds with varying cerium doping levels on hBMSCs using nanoparticle-hybridized hydrogel scaffold extracts as the experimental groups and osteogenic medium

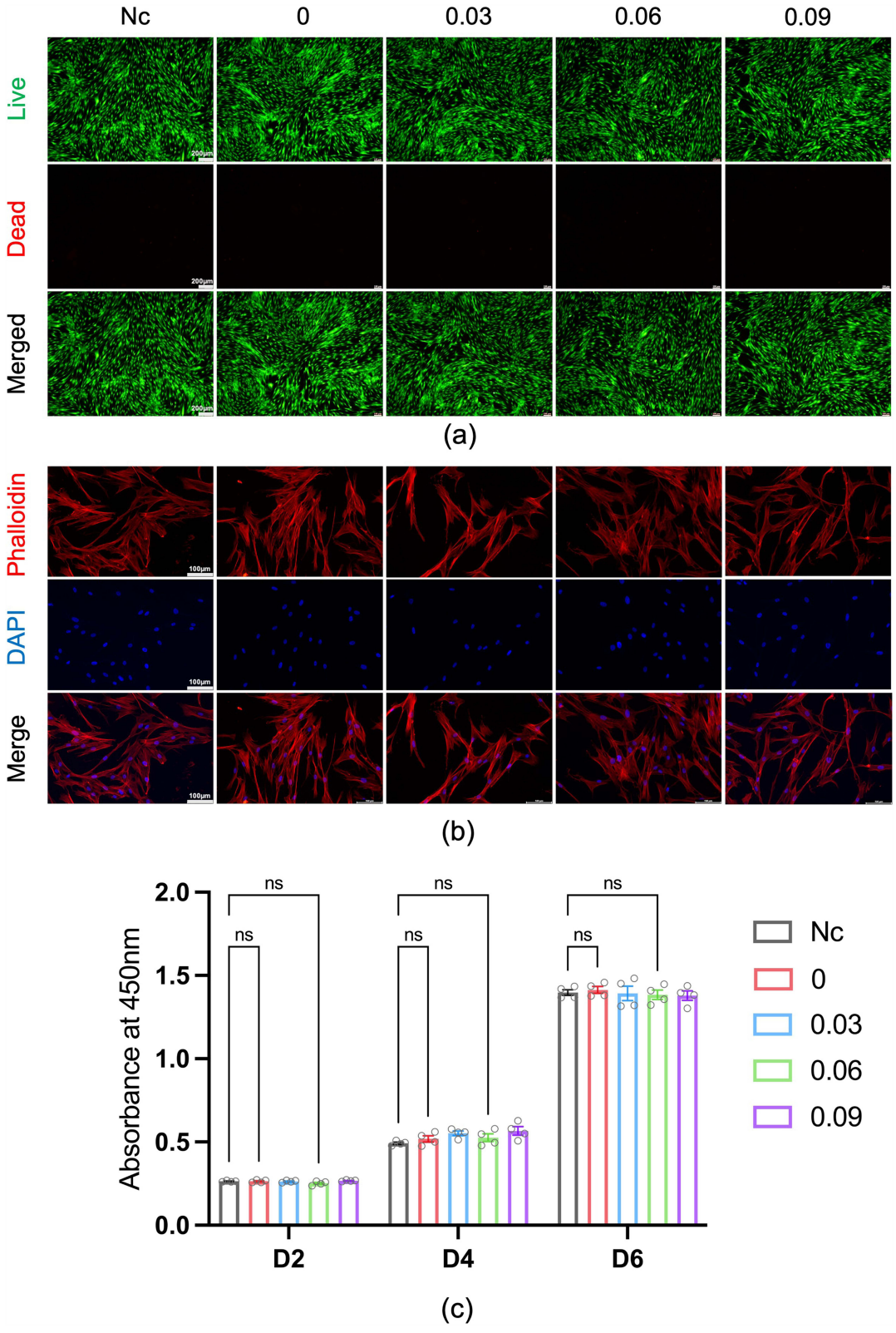

Figure 4 Biocompatibility evaluation of composite scaffolds. (**a**) Live/Dead cell staining and (**b**) phalloidin-DAPI staining of hBMSCs cultured with scaffold extracts at day 3 (nuclei – blue, cytoskeleton – red). (**c**) the proliferation of hBMSCs cultured with different scaffolds using CCK-8 assay.

https://doi.org/10.2147/IJN.S514047

(OM) as the control group. Alkaline phosphatase (ALP), an early marker of osteogenic differentiation, was assessed after 7 days of osteogenic induction. The results of ALP staining are shown in Figure 5a. Distinct differences in staining intensity were observed among the groups. The Nc group exhibited the lightest staining, indicating lower osteogenic activity, whereas the addition of inorganic nanoparticles in the experimental groups significantly enhanced the osteogenic activity of hBMSCs. Groups 0 and 0.03 showed deeper staining intensities compared to the Nc group, likely due to the combined effects of Ca, Mg, and Ce ions and the bioelectric activity of the scaffolds. Groups 0.06 and 0.09 exhibited the most intense staining, suggesting a further enhancement of osteogenic activity with increasing cerium content. To assess mineralization at later stages of differentiation, alizarin red staining (ARS) was performed after 14 days of osteogenic induction (Figure 5a). The experimental groups showed higher calcium nodule deposition compared to the Nc group.

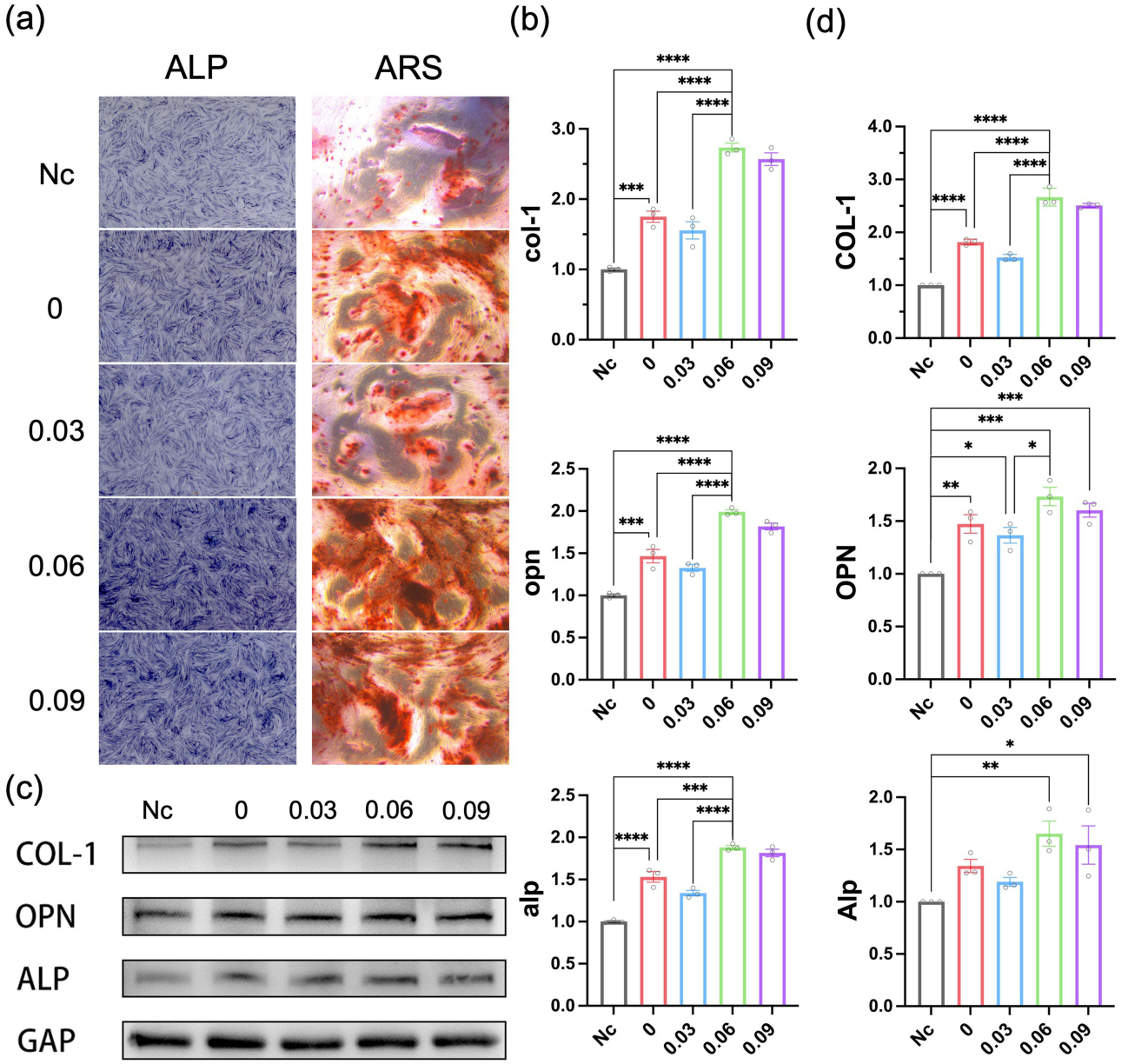

Figure 5 Evaluation for the effect of various mediums on osteogenic differentiation. (**a**) ALP staining of hBMSCs cultured with scaffold extracts for 7 days and ARS staining of hBMSCs cultured with scaffold extracts for 14 days. (**b**) osteogenic gene expression levels (col-1, opn, and alp) for hBMSCs after 7 days of osteogenic induction. (**c**) immunoblot of osteogenic proteins (COL-1, OPN, and ALP) images and (**d**) corresponding quantitative data for hBMSCs after various OM stimulation for 7 days in each group. (n = 3, *p < 0.05, **p < 0.01, ***p < 0.001, and ****p < 0.0001).

Groups 0.06 and 0.09 demonstrated the most prominent ARS activity, evident from the darkest red staining and the greatest deposition of calcium nodules. This trend was consistent with the ALP staining results.

To further explore differences in osteogenic effects among the groups at the gene and protein expression levels, RT-qPCR and Western blotting were performed on cells after 7 days of osteogenic induction. As shown in Figure 5b, the expression levels of osteogenesis-related genes (col-1, opn, and alp) were higher in all four scaffold material groups compared to the Nc group, demonstrating that the incorporation of nanoparticles enhanced osteogenic activity across all experimental groups. Group 0 exhibited a significant increase in gene expression relative to the Nc group, likely due to the release of Ca^{2+} and Mg^{2+} ions from the scaffold material and the associated bioelectric activity, which strongly promoted osteogenic differentiation. In contrast, group 0.03 showed a slight decline in gene expression, which may be attributed to the incorporation of cerium elements that potentially reduce the electroactivity of pWH, thereby reducing the overall osteogenic effect of the scaffold. Interestingly, although the electrical activity of the scaffold material decreased with increasing cerium doping, the osteogenic-promoting effects of cerium itself gradually compensated for, and eventually outweighed, the reduced electroactivity at higher doping levels. This trend was most pronounced in group 0.06, which showed a significant improvement in osteogenic activity. However, when the cerium content was further increased (group 0.09), a slight decline in osteogenic activity was observed compared to group 0.06.

We propose that an excessive addition of cerium may have reduced the crystallinity of the nanoparticles, thereby weakening their osteoconductivity to some extent. This hypothesis aligns with findings from YiHuan et al, who highlighted the critical role of size, shape, and crystallinity of nanomaterials in determining their biocompatibility and osteogenic performance.[61] Furthermore, a 2007 study demonstrated that the crystalline phase of calcium phosphate (HAP) provided a superior matrix for BMSCs compared to the amorphous phase (ACP) when size effects were excluded.[62] Consistent with the RT-qPCR results, protein blotting analysis and corresponding quantitative data for osteogenesis-related proteins (COL-1, OPN, and ALP) in each group (Figure 5c and d) confirmed similar trends. These findings collectively suggest that group 0.06 scaffolds exhibit optimal properties for promoting osteogenic activity. Based on these results, it is reasonable to expect that the group 0.06 scaffold will perform effectively in in situ bone regeneration tests.

Animal Experiments

The in vitro studies demonstrated that the developed scaffold materials not only possess excellent biocompatibility but also exhibit varying osteogenic activities depending on the concentration of cerium doping. To validate these findings, complementary in vivo experiments were conducted. Based on the encouraging in vitro results, a circular critical bone defect model with a 5 mm diameter was established in the cranial bones of rats, and new bone formation was analyzed using micro-computed tomography (micro-CT). Figure 6a depicts the modeling process, and reconstructed micro-CT three-dimensional (3D) images of each group at 4 weeks (4W) and 8 weeks (8W) post-implantation are shown in Figure 6b. A significant increase in new bone formation was observed in all groups at 8W compared to 4W. In the Nc group, new bone formation was limited to the marginal region of the defect, with the central hollow area still visible at 8W. In contrast, the other four groups exhibited varying degrees of new bone formation within the central region of the defect. As expected, groups 0.06 and 0.09 showed the most significant new bone formation. Quantitative analysis of bone volume/tissue volume (BV/TV) and local bone mineral density (BMD) (Figure 6c) provided further insights. Group 0.06 displayed the highest BV/TV and BMD values among all groups, reaching 72.50% and 0.78 g/cm³ at 8W, exceeding the Nc group by more than 2.5 times. The trends in BV/TV and BMD data were consistent across both time points, with similar patterns evident in visual images and quantitative analyses. These results align well with the trends observed in in vitro experiments, reinforcing the conclusion that the group 0.06 scaffold exhibits superior osteogenic performance.

After implanting the various scaffolds into cranial defects, Figure 7 presents H&E-stained images at 4 and 8 weeks post-implantation. In the Nc group at 4 weeks post-operation, the defect site was dominated by inflammatory cells and extracellular matrix, with no evidence of newly formed bone tissue. In contrast, the other groups showed varying degrees of bone tissue formation (indicated by black arrows), reflecting the excellent histocompatibility and osteogenic potential of scaffolds containing different inorganic nanoparticles. Among these, group 0.06 demonstrated the most substantial new bone formation. At 8 weeks post-operation, all groups exhibited significantly more bone tissue formation at the

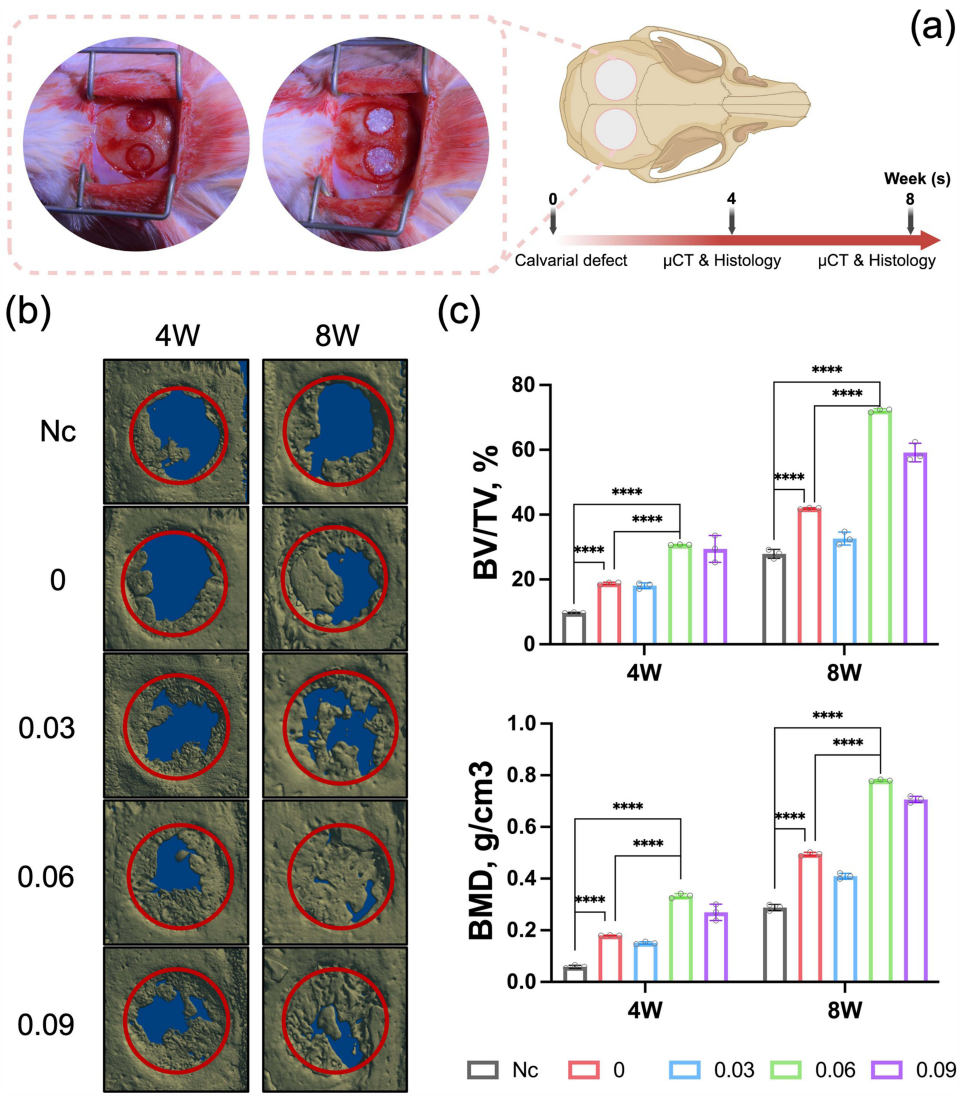

Figure 6 Evaluation of bone regeneration of various scaffolds after implantation. (**a**) schematic illustrating the establishment of 5-mm diameter circular bone defect in the skull of SD rats and the implantation of various scaffolds. (**b**) reconstructed micro-CT images of rat calvaria at 4 W and 8 W post-implantation, and (**c**) corresponding quantitative analysis of BV/TV and BMD. (n = 3, ****p < 0.0001).

defect site compared to 4 weeks. Masson's trichrome staining, a widely used method for visualizing collagen fibers with distinctive color contrast, further confirmed these findings. As shown in Figure 7, the blue staining, indicative of rich collagen deposition and newly formed bone tissue, was least pronounced in the Nc group. Groups 0.06 and 0.09 displayed the highest intensity of blue staining. At 8 weeks, red staining in the images denoted mature bone tissue, corresponding to the organization of calcified extracellular matrix. The Nc group showed the least red staining, while groups 0 and 0.03 displayed slightly higher levels. Group 0.06 exhibited the most pronounced red staining, indicating extensive mature bone formation. Immunohistochemical staining for OPN yielded similar results. At 4 weeks post-implantation, positive staining for osteoblasts and new bone was significantly greater in the experimental groups than in the Nc group, with group 0.06 showing the darkest staining. These findings were consistent with the results of RT-qPCR and Western blotting (Figure 5b–d). By 8 weeks, as mature bone tissue formed, groups 0.06 and 0.09 exhibited the greatest amount of mature bone (indicated by black triangles), along with significant positive staining. The results demonstrate that, without the addition of exogenous cells or growth factors, group 0.06 exhibited the best osteogenic effect among all groups in both in vitro and in vivo experiments. These findings highlight the excellent biocompatibility and substantial repair capability of the developed scaffolds for restoring critical-size bone defects.

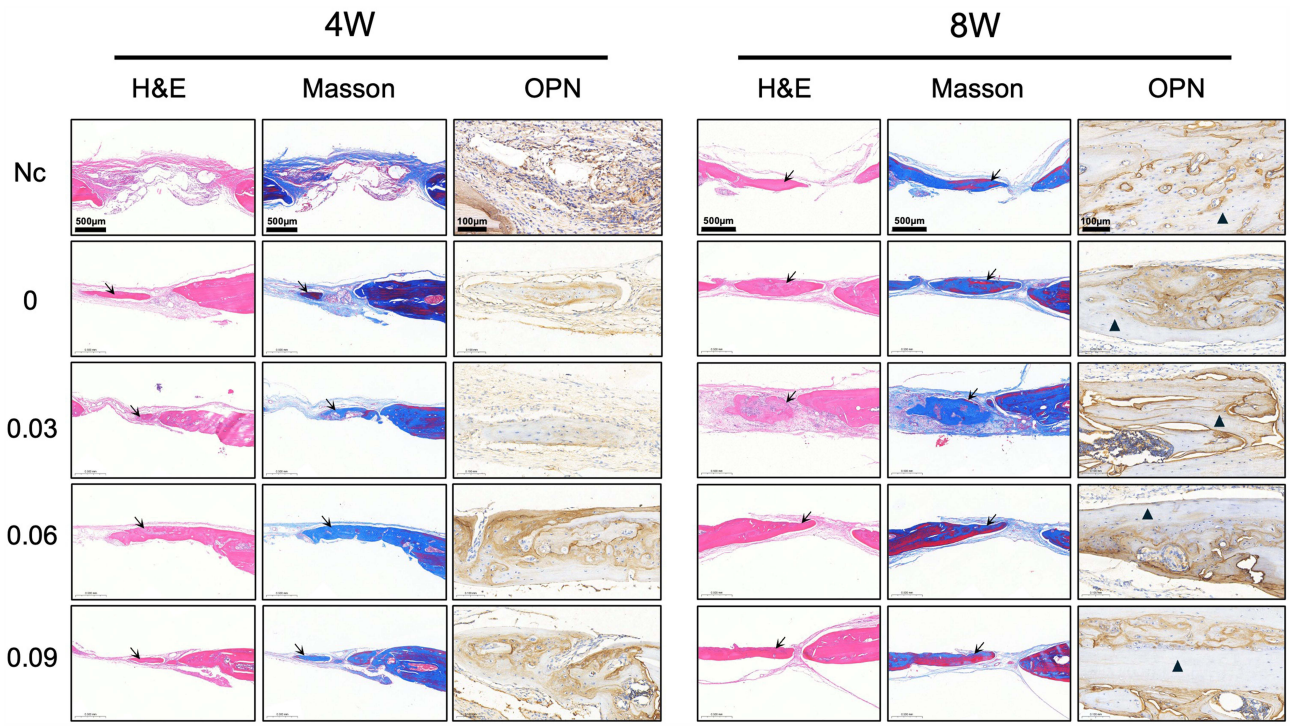

Figure 7 Histological analysis. H&E staining, Masson's trichrome staining, and Immunohistochemical staining of OPN expression at 4 W and 8 W post-implantation.

Conclusion

This study investigated the effects of varying Ce doping levels on the osteogenic properties and biosafety of pWH nanoparticle materials. Nanoparticles were successfully synthesized via chemical precipitation and annealed to impart piezoelectric properties. For the development of bone tissue engineering scaffolds, inorganic nanoparticle-doped, freeze-dried hydrogel scaffolds capable of continuously releasing bioactive ions while maintaining piezoelectricity were successfully fabricated. A comprehensive characterization of the scaffold materials, along with ex vivo validation experiments, was conducted. The results demonstrated that all nanohybrid scaffolds exhibited excellent biocompatibility, were non-toxic to hBMSCs and bone tissues, and confirmed that Ce doping significantly influenced the osteogenic properties of pWH-based scaffolds. Importantly, an optimal doping level was identified, which enhanced both in vitro and in vivo bone regeneration. These findings establish Ce-doped pWH scaffolds as a promising material for bone tissue engineering applications, with the identified optimal Ce/Ca ratio providing valuable guidance for future scaffold development. It is noteworthy that the osteogenic activity of the nanoparticle hybrid scaffolds with electroactive nanoparticles did not continuously increase with the addition of Ce at safe concentrations. This highlights the importance of carefully considering the interactions between multiple bioactive materials. Identifying the underlying principles and utilizing synergistic effects, while avoiding antagonistic interactions, is essential for achieving desired outcomes in bone tissue engineering.

Ethical Approval

The Animal Ethical and Welfare Committee of Nanjing Medical University reviewed and approved the animal study.

Funding

The study is funded by the Chinese National Natural Science Foundation (81670967).

Disclosure

The authors declare that they have no conflict of interest. Graphical abstract Created in BioRender. C Niecy, C. (2024) https://BioRender.com/o02q776

References

1. Koushik TM, Miller CM, Antunes E. Bone tissue engineering scaffolds: function of multi-material hierarchically structured scaffolds. *Adv Healthcare Mater*. 2023;12(9). doi:10.1002/adhm.202202766
2. Sun X, Jiao X, Wang Z, et al. Polydopamine-coated 3D-printed β-tricalcium phosphate scaffolds to promote the adhesion and osteogenesis of BMSCs for bone-defect repair: mRNA transcriptomic sequencing analysis. *J Mat Chem B*. 2023;11(8):1725–1738. doi:10.1039/D2TB02280J
3. Huang X, Lou Y, Duan Y, et al. Biomaterial scaffolds in maxillofacial bone tissue engineering: a review of recent advances. *Bioact Mater*. 2024;33:129–156. doi:10.1016/j.bioactmat.2023.10.031
4. Zhou X, Qian Y, Chen L, et al. Flowerbed-inspired biomimetic scaffold with rapid internal tissue infiltration and vascularization capacity for bone repair. *ACS Nano*. 2023;17(5):5140–5156. doi:10.1021/acsnano.3c00598
5. Aghajanzadeh MS, Imani R, Nazarpak MH, et al. Augmented physical, mechanical, and cellular responsiveness of gelatin-aldehyde modified xanthan hydrogel through incorporation of silicon nanoparticles for bone tissue engineering. *Int J Biol Macromol*. 2024;259:129231. doi:10.1016/j.ijbiomac.2024.129231
6. Schulze F, Lang A, Schoon J, et al. Scaffold guided bone regeneration for the treatment of large segmental defects in long bones. *Biomedicines*. 2023;11:325. doi:10.3390/biomedicines11020325
7. Sallent I, Capella-Monsonís H, Procter P, et al. The few who made it: commercially and clinically successful innovative bone grafts. *Front Bioeng Biotechnol*. 2020;8. doi:10.3389/fbioe.2020.00952
8. Vukicevic S, Oppermann H, Verbanac D, et al. The clinical use of bone morphogenetic proteins revisited: a novel biocompatible carrier device OSTEOGROW for bone healing. *Int Orthop*. 2014;38(3):635–647. doi:10.1007/s00264-013-2201-1
9. Heng C, Zheng X, Hui J, et al. Neodymium and manganese ions co-doped whitlockite for temperature monitoring, photothermal therapy, and bone tissue repair in osteosarcoma. *J Colloid Interface Sci*. 2024;653:1488–1503. doi:10.1016/j.jcis.2023.09.186
10. Jeong J, Shim JH, Heo CY. The effects of local treatment of PTH(1-34) and whitlockite and hydroxyapatite graft to the calvarial defect in a rat osteoporosis model. *Biomedicines*. 2024;12(4):820. doi:10.3390/biomedicines12040820
11. Jang HL, Jin K, Lee J, et al. Revisiting whitlockite, the second most abundant biomineral in bone: nanocrystal synthesis in physiologically relevant conditions and biocompatibility evaluation. *ACS Nano*. 2013;8(1):634–641. doi:10.1021/nn405246h
12. Yang Z, Yao T, Zheng X, et al. Eu3+/Tb3+-doped whitlockite nanocrystals: controllable synthesis, cell imaging, and the degradation process in the bone reconstruction. *Nano Res*. 2022;15(2):1303–1309. doi:10.1007/s12274-021-3654-y
13. Kim HD, Jang HL, Ahn HY, et al. Biomimetic whitlockite inorganic nanoparticles-mediated in situ remodeling and rapid bone regeneration. *Biomaterials*. 2017;112:31–43. doi:10.1016/j.biomaterials.2016.10.009
14. Wang C, Jeong K-J, Park HJ, et al. Synthesis and formation mechanism of bone mineral, whitlockite nanocrystals in tri-solvent system. *J Colloid Interface Sci*. 2020;569:1–11. doi:10.1016/j.jcis.2020.02.072
15. Hu M, Xiao F, Ke QF, et al. Cerium-doped whitlockite nanohybrid scaffolds promote new bone regeneration via SMAD signaling pathway. *Chem Eng J*. 2019;359:1–12. doi:10.1016/j.cej.2018.11.116
16. Sevari SP, Kim JK, Chen C, et al. Whitlockite-enabled hydrogel for craniofacial bone regeneration. *ACS Appl Mater Interfaces*. 2021;13(30):35342–35355. doi:10.1021/acsami.1c07453
17. Xiao F, Shi JJ, Zhang XH, et al. Gadolinium-doped whitlockite/chitosan composite scaffolds with osteogenic activity for bone defect treatment: in vitro and in vivo evaluations. *Front Bioeng Biotechnol*. 2023;11. doi:10.3389/fbioe.2023.1071692
18. Liu Q, Kim JH, Cho M, et al. Bioactive magnesium-based whitlockite ceramic as bone cement additives for enhancing osseointegration and bone regeneration. *Mater Des*. 2023;229:111914. doi:10.1016/j.matdes.2023.111914
19. Jeong J, Shim JH, Koo BM, et al. Synergistic effect of whitlockite scaffolds combined with alendronate to promote bone regeneration. *Tissue Eng and Regener Med*. 2022;19(1):83–92. doi:10.1007/s13770-021-00416-2
20. Chang Y, Zhao R, Wang H, et al. A novel injectable whitlockite-containing borosilicate bioactive glass cement for bone repair. *J Non-Crystalline Solids*. 2020;547:120291. doi:10.1016/j.jnoncrysol.2020.120291
21. Amirthalingam S, Ramesh A, Lee SS, et al. Injectable in situ shape-forming osteogenic nanocomposite hydrogel for regenerating irregular bone defects. *ACS Appl Bio Mater*. 2018;1(4):1037–1046. doi:10.1021/acsabm.8b00225
22. Wang L, Pang Y, Tang Y, et al. A biomimetic piezoelectric scaffold with sustained Mg2+ release promotes neurogenic and angiogenic differentiation for enhanced bone regeneration. *Bioact Mater*. 2023;25:399–414. doi:10.1016/j.bioactmat.2022.11.004
23. Li Q, Liu W, Hou W, et al. Micropatterned photothermal double-layer periosteum with angiogenesis-neurogenesis coupling effect for bone regeneration. *Mater Today Bio*. 2023;18:100536. doi:10.1016/j.mtbio.2022.100536
24. Chandran RR, Elakkiya K, Bargavi P, et al. Evaluation of whitlockite through conventional hydrothermal method and its in-vitro erythrocyte compatibility and antibacterial activity. *AIP Conf Proc*. 2020;2265(1):030235. doi:10.1063/5.0017563
25. Muthiah Pillai NS, Eswar K, Amirthalingam S, et al. Injectable nano whitlockite incorporated chitosan hydrogel for effective hemostasis. *ACS Appl Bio Mater*. 2019;2(2):865–873. doi:10.1021/acsabm.8b00710
26. Kumar N, Bose P, Kumar S, et al. Nanoapatite-Loaded κ-Carrageenan/Poly(vinyl alcohol)-based injectable cryogel for hemostasis and wound healing. *Biomacromolecules*. 2024;25(2):1228–1245. doi:10.1021/acs.biomac.3c01180
27. Jang HL, Zheng GB, Park J, et al. In vitro and in vivo evaluation of whitlockite biocompatibility: comparative study with hydroxyapatite andβ-tricalcium phosphate. *Adv Healthcare Mater*. 2016;5(1):128–136. doi:10.1002/adhm.201400824
28. Jang HL, Lee HK, Jin K, et al. Phase transformation from hydroxyapatite to the secondary bone mineral, whitlockite. *J Mat Chem B*. 2015;3(7):1342–1349. doi:10.1039/c4tb01793e
29. Bauer L, Antunović M, Rogina A, et al. Bone-mimetic porous hydroxyapatite/whitlockite scaffolds: preparation, characterization and interactions with human mesenchymal stem cells. *J Mater Sci*. 2021;56(5):3947–3969. doi:10.1007/s10853-020-05489-3
30. Liu H, Shi Y, Zhu Y, et al. Bioinspired piezoelectric periosteum to augment bone regeneration via synergistic immunomodulation and osteogenesis. *ACS Appl Mater Interfaces*. 2023;15(9):12273–12293.
31. Zheng TY, Zhao H, Huang YQ, et al. Piezoelectric calcium/manganese-doped barium titanate nanofibers with improved osteogenic activity. *Ceram Int*. 2021;47(20):28778–28789. doi:10.1016/j.ceramint.2021.07.038

32. Mohamed Mustakim NS, Kamaruzaman D, Abdullah MH, et al. Review of recent advances in piezoelectric material for nanogenerator application: preparation methods, material selection, performance, applications, and future outlook. *J Mater Sci*. 2024;59(41):19380–19423. doi:10.1007/s10853-024-10293-4
33. Kaliannagounder VK, Raj NP, Unnithan AR, et al. Remotely controlled self-powering electrical stimulators for osteogenic differentiation using bone inspired bioactive piezoelectric whitlockite nanoparticles. *Nano Energy*. 2021;85:105901. doi:10.1016/j.nanoen.2021.105901
34. Jacob J, More N, Kalia K, et al. Piezoelectric smart biomaterials for bone and cartilage tissue engineering. *Inflamm Regen*. 2018;38(1). doi:10.1186/s41232-018-0059-8
35. Kapat K, Shubhra QTH, Zhou M, et al. Piezoelectric nano-biomaterials for biomedicine and tissue regeneration. *Adv Funct Mater*. 2020;30(44):1909045. doi:10.1002/adfm.201909045
36. Huang Y, Zhai X, Ma T, et al. Rare earth-based materials for bone regeneration: breakthroughs and advantages. *Coord Chem Rev*. 2022;450:214236. doi:10.1016/j.ccr.2021.214236
37. Hu Y, Du Y, Jiang H, et al. Cerium promotes bone marrow stromal cells migration and osteogenic differentiation via Smad1/5/8 signaling pathway. *Int J Clin Exp Pathol*. 2014;7(8):5369–5378.
38. Xu C, Qu X. Cerium oxide nanoparticle: a remarkably versatile rare earth nanomaterial for biological applications. *Npg Asia Materials*. 2014;6(3):e90–e90. doi:10.1038/am.2013.88
39. Kim YG, Lee Y, Lee N, et al. Ceria-Based Therapeutic Antioxidants for Biomedical Applications. *Adv Mater*. 2023;36(10). doi:10.1002/adma.202210819
40. Yadav S, Chamoli S, Kumar P, et al. Structural and functional insights in polysaccharides coated cerium oxide nanoparticles and their potential biomedical applications: a review. *Int J Biol Macromol*. 2023;246:125673. doi:10.1016/j.ijbiomac.2023.125673
41. Purohit SD, Singh H, Bhaskar R, et al. Gelatin—alginate—cerium oxide nanocomposite scaffold for bone regeneration. *Mater Sci Eng C*. 2020;116:111111. doi:10.1016/j.msec.2020.111111
42. Kalyanaraman V, Naveen SV, Mohana N, et al. Biocompatibility studies on cerium oxide nanoparticles – combined study for local effects, systemic toxicity and genotoxicity via implantation route. *Toxicol Res*. 2019;8(1):25–37. doi:10.1039/c8tx00248g
43. Xu C, Lin Y, Wang J, et al. Nanoceria-triggered synergetic drug release based on CeO2-Capped mesoporous silica host–guest interactions and switchable enzymatic activity and cellular effects of CeO2 nanoceria-triggered synergetic drug release based on CeO_2-Capped mesoporous silica host-guest interactions and switchable enzymatic activity and cellular effects of CeO_2. *Adv Healthcare Mater*. 2013;2(12):1591–1599. doi:10.1002/adhm.201200464
44. Li K, Yu J, Xie Y, et al. The effects of cerium oxide incorporation in calcium silicate coating on bone mesenchymal stem cell and macrophage responses. *Biol Trace Elem Res*. 2017;177(1):148–158. doi:10.1007/s12011-016-0859-0
45. Xiang J, Li J, He J, et al. Cerium oxide nanoparticle modified scaffold interface enhances vascularization of bone grafts by activating calcium channel of mesenchymal stem cells. *ACS Appl Mater Interfaces*. 2016;8(7):4489–4499. doi:10.1021/acsami.6b00158
46. Zhang M, Zhai X, Ma T, et al. Sequential Therapy for Bone Regeneration by Cerium Oxide-Reinforced 3D-Printed Bioactive Glass Scaffolds. *ACS Nano*. 2023;17(5):4433–4444. doi:10.1021/acsnano.2c09855
47. Thangaraju P, Varthya SB. ISO 10993: biological evaluation of medical devices. In: Shanmugam PST, Thangaraju P, Palani N, Sampath T, editors. *Medical Device Guidelines and Regulations Handbook*. Cham: Springer International Publishing; 2022:163–187.
48. Mao Q, Zhu B, Zhuang H, et al. 3D-printing assisted SF-SA based mgp hybrid hydrogel scaffold for bone tissue engineering. *Front Mater*. 2022;9. doi:10.3389/fmats.2022.896516
49. Zheng ALT, Sinin AE, Jin WT, et al. Rare earth elements for enhancing photocatalysis in pollutant degradation and water treatment. *Int J Environ Sci Technol*. 2024. doi:10.1007/s13762-024-06203-5
50. Fan Y, Jia Z, Zhang Z, et al. Flexible composites with rare-earth element doped polycrystalline particles for piezoelectric nanogenerators. *Micromachines*. 2024;15:1280. doi:10.3390/mi15111280
51. Wang M, Yao J, Shen S, et al. A scaffold with zinc-whitlockite nanoparticles accelerates bone reconstruction by promoting bone differentiation and angiogenesis. *Nano Res*. 2023;16(1):757–770. doi:10.1007/s12274-022-4644-4
52. Radulescu D-E, Vasile OR, Andronescu E, et al. Latest research of doped hydroxyapatite for bone tissue engineering. *Int J Mol Sci*. 2023;24:13157. doi:10.3390/ijms241713157
53. Ali F, Khalid NR, Nabi G, et al. Hydrothermal synthesis of cerium-doped CoO nanoflakes as electrode for supercapacitor application hydrothermal synthesis of cerium-doped. *Int J Energy Res*. 2021;45(2):1999–2010. doi:10.1002/er.5893
54. Pitcheri R, Mooni SP, Radhalayam D, et al. Effect of Ce-doping on the structural, morphological, and electrochemical features of Co3O4 nanoparticles synthesized by solution combustion method for battery-type supercapacitors. *Ceram Int*. 2024;50(23):50504–50515. doi:10.1016/j.ceramint.2024.09.396
55. Tan J, Huang R, Lin H-T, et al. Enhancement of piezoelectric properties of CaBi2Nb2O9 ceramics by Ce doping and direct reaction sintering. *Ceram Int*. 2024;50(14):25801–25809. doi:10.1016/j.ceramint.2024.04.317
56. Wei J, Xia J, Liu X, et al. Hollow-structured BaTiO3 nanoparticles with cerium-regulated defect engineering to promote piezocatalytic antibacterial treatment. *Appl Catal B*. 2023;328:122520. doi:10.1016/j.apcatb.2023.122520
57. Yang Y, Sun E, Xu Z, et al. Sm and Mn co-doped PMN-PT piezoelectric ceramics: defect engineering strategy to achieve large d33 and high Qm. *J Mater Sci Technol*. 2023;137:143–151. doi:10.1016/j.jmst.2022.08.004
58. Guo X, Li X, Lei J, et al. Improved piezoelectric and photoluminescence properties in Ce-doped PSN-PMN-PT piezoelectric ceramics by multiscale coordination. *Ceram Int*. 2024;50(19):35638–35646. doi:10.1016/j.ceramint.2024.06.380
59. Jana S, Florczyk SJ, Leung M, et al. High-strength pristine porous chitosan scaffolds for tissue engineering. *J Mater Chem*. 2012;22(13):6291. doi:10.1039/c2jm16676c
60. Zhang J, Tang L, Qi H, et al. Dual function of magnesium in bone biomineralization. *Adv Healthcare Mater*. 2019;8(21):1901030. doi:10.1002/adhm.201901030
61. Yi H, Ur Rehman F, Zhao C, et al. Recent advances in nano scaffolds for bone repair. *Bone Res*. 2016;4(1). doi:10.1038/boneres.2016.50
62. Hu Q, Tan Z, Liu Y, et al. Effect of crystallinity of calcium phosphate nanoparticles on adhesion, proliferation, and differentiation of bone marrow mesenchymal stem cells. *J Mater Chem*. 2007;17(44):4690–4698. doi:10.1039/B710936A